Marine and Petroleum Geology 112 (2020) 104042

Contents lists available at ScienceDirect

Marine and Petroleum Geology

journal homepage: www.elsevier.com/locate/marpetgeo

Research paper

Determination of the critical flow pore diameter of shale caprock

Cunfei Ma[a,b,c,d,e,*], Chengyan Lin[a,b,c,d], Chunmei Dong[a,b,c,d], Derek Elsworth[f], Songtao Wu[g], Xiaoqi Wang[g], Xiaolong Sun[a]

[a] School of Geosciences in China University of Petroleum East China, Qingdao, 266580, China
[b] Key Laboratory of Deep Oil & Gas Geology and Geophysics (China University of Petroleum), Ministry of Education, Qingdao, 266580, China
[c] Reservoir Geology Key Laboratory of Shandong Province(East China), Qingdao, 266580, China
[d] Research Laboratory of China University of Petroleum(East China), Key Laboratory of Oil and Gas Reservoir of China National Petroleum Corporation, Qingdao, 266580, China
[e] Key Laboratory of Shale Oil and Gas Exploration & Production, SINOPEC, Dongying, 257100, China
[f] The Pennsylvania State University (University Park), State College, PA, 16803, USA
[g] Research Institute of Petroleum Exploration and Development (RIPED), Beijing, 100000, China

ARTICLE INFO

Keywords:
Shale caprock
Breakthrough pressure limit
Critical lithology
Critical flow pore diameter
Unconventional reservoir test technology

ABSTRACT

The breakthrough pressure and pore permeability characteristics of shale caprock are the physical response of the microscopic pore throat structure. Whether oil and gas can break through shale caprock under the action of migration force is closely related to the critical flow pore diameter (pore throat diameter) of the rock. Therefore, the critical flow pore diameter is a key parameter for the division of the reservoir and caprock and evaluation of the physical seal abilities of caprock, affecting the oil and gas migration and accumulation, which are controlled by the critical lithology. In this study, the shale caprock of the N gas reservoir of the Huagang Formation in the Xihu sag, East China Sea Basin was comprehensively studied using particle size analysis, systematic environmental scanning electron microscopy, nano-CT, digital core reconstruction, low-temperature gas adsorption, high-pressure mercury intrusion, and nuclear magnetic resonance test for unconventional reservoir. In addition, the critical flow pore diameter of the shale caprock was determined. Based on the intersection point of the trendline of the breakthrough pressure data between the caprock and reservoir and the lower breakthrough pressure limit of the caprock of the gas–water reservoir, the breakthrough pressure limit of the caprock and reservoir is 2 MPa. Based on the correlation between the breakthrough pressure and shale lithology, the critical lithology for the division of the caprock and reservoir is argillaceous siltstone with a low breakthrough pressure limit of 2 MPa. Based on the identification of lithology boundary between caprock and reservoir, the critical lithology of the argillaceous siltstone selected as the research object, above-mentioned unconventional reservoir test technologies were carried out. The pore size statistics obtained from environmental scanning electron microscopy and the digital core model show that the critical flow pore diameter is between 100 and 300 nm. The high-pressure mercury injection test shows that the critical flow pore diameter ≥155 nm. The full pore diameter distribution curve is obtained by combined low-temperature carbon dioxide adsorption, low-temperature nitrogen adsorption and high-pressure mercury injection measurements. Compared the full pore diameter distribution curve with the nuclear magnetic resonance T2 spectrometry before and after centrifugation, the critical flow pore diameter is greater than 84 nm, ranging between 148 and 339 nm. Finally, based on the lithology, breakthrough pressure, and pore diameter relationships, the critical flow pore diameter of the shale caprock is 200 nm.

1. Introduction

The critical flow pore diameter refers to the minimum pore throat diameter of a rock pore throat network, which can store hydrocarbon and make hydrocarbon seepage (Bai et al., 2014). Current research methods that can be used to determine the critical flow pore diameter can be divided into three categories: physical property low-limit calibrations, theoretical derivations, and experimental tests.

During the development of oil and gas fields, it is necessary to determine the physical property boundaries between effective reservoirs

* Corresponding author. School of Geosciences in China University of Petroleum East China, Qingdao, 266580, China.
E-mail address: mcf-625@163.com (C. Ma).

https://doi.org/10.1016/j.marpetgeo.2019.104042
Received 12 May 2019; Received in revised form 9 September 2019; Accepted 9 September 2019
Available online 10 September 2019
0264-8172/

and non-reservoirs (Stout, 1964; Jiao et al., 2009; Wang, 2009; Li et al., 2014) including the lower boundaries of the porosity and permeability, which are usually obtained by statistical analysis of the physical properties or based on the oil-bearing occurrences of the samples (Lu et al., 2012; Zou et al., 2013). The critical flow pore diameter can be obtained by calibrating the pore size test data and formula calculation (Purcell, 1949; Yan et al., 2018).

The theoretical derivation method is a mathematical method, which is based on the mechanical balance of oil and gas filling. Starting from the force exerted during oil and gas filling, the mathematical model for the critical flow pore diameter was established by using the Young-Laplace equation (Gee et al., 1990). It is based on the principle that the dynamic force and resistance are equal when the oil and gas filling is balanced. Based on the maximum filling near the source reservoir interface and in the reservoir interior, a theoretical model for the critical flow pore diameter was established (Zhang et al., 2014a, 2014b). Deng et al. (2018) further used the formation fracture pressure to determine the critical flow pore diameter. The theoretical derivation method is significant because it can be used to determine the critical flow pore diameter based on the oil and gas filling mechanics. However, the mineral compositions and pore structures of the reservoirs are not analyzed in detail and actual data are not supported.

Experimental methods include the capillary pressure curve method, bound water film thickness method, scanning electron microscopy, nuclear magnetic resonance (NMR) T2 spectrum method, and oil content method. The principle of the capillary pressure curve method is that the amount of mercury inflow in different pressure intervals represents the volume of an interconnected pore throat system with similar pore throat sizes. The cumulative mercury saturation and permeability contribution values of each core were used to draw correlation curves. Several straight lines appear in the curves, representing different pore throat systems in the cores. The cumulative permeability contribution curve shows the contribution of the pore throat system to the core permeability. The pore throat system with the largest pore diameter contributes most to the core permeability. When the cumulative permeability reaches 99.99%, the corresponding pore diameter is the critical flow pore diameter of the gas reservoir (Purcell, 1949). The J-function method can be used to reflect the real reservoir performance and microheterogeneity and to eliminate the influence of the porosity and permeability on the capillary pressure. The relationship between the J-function and capillary pressure can be obtained (Leverett, 1941; Gao et al., 2011; Hu et al., 2012; Liu et al., 2016; Alyafei and Blunt, 2018). Subsequently, the contribution value and cumulative permeability of each pore volume interval can be calculated (Purcell, 1949) and the critical flow pore diameter can be obtained by drawing curves.

When oil and gas accumulate in tight reservoirs, it is impossible for oil and gas to completely displace the water from the pores and produce a bound water film because of the capillary force, fluid wettability, and attraction between fluid and solid molecules. When the pore size equals the total thickness of the bound water film, the fluid begins to flow and the corresponding pore size is the critical flow pore diameter (He and Hua, 1998; Xiang et al., 1999; Gao et al., 2011; Zou et al., 2011; Cao et al., 2013; Yang et al., 2013; P. Zhang et al., 2019). Therefore, the critical flow pore diameter can be obtained by measuring or calculating the thickness of the bound water film. At present, the most commonly used method is the bound water film thickness method combined with the particle sizes of the molecular oil and gas aggregates. First, the bound water film thickness is calculated based on the measured bound water saturation, rock specific surface, and rock density data. Subsequently, the critical flow pore diameter is determined (Zou et al., 2011, 2013) by adding the particle sizes of the molecular crude oil aggregates.

If the power is insufficient when the hydrocarbon migrates along the pore throat, the migration stops, leading to different oil contents at both ends of the pore throat. If one side of the pore throat contains hydrocarbon residue but there is no hydrocarbon residue on the adjacent side of the same pore throat, the critical flow pore diameter is between the two pore sizes. The pore size interval value is then gradually narrowed down, measured repeatedly, and gradually approached. Finally, the critical flow pore diameter (Zou et al., 2013) can be obtained. The critical flow pore diameter obtained by environmental scanning electron microscopy (ESEM) has a high reliability, but this method requires representative and universal samples and correct operation.

The NMR is a physical process in which the nucleus of a substance interacts with a magnetic field. Because the length of the transverse relaxation time (T2) of hydrogen nuclei corresponds to the size of the pore space, it reflects the pore throat structure characteristics. Therefore, the T2 distribution can be used to describe the pore diameter distribution. Generally, the first peak is considered to reflect a bound pore that is occupied by bound fluid in a bound or immobile state, while the second peak reflects a movable pore that is occupied by movable fluid in a free or flowable state (Ren et al., 2017). The corresponding pore size is the lower limit of the movable fluid pore size, which can be considered as critical flow pore size. A pore throat smaller than the pore size is occupied by bound water. At the same time, there is a good correlation between the capillary pressure curve and NMR T2 spectrum, which can be overlapped by translation or mathematical transformation. The pore size distribution of movable and bound fluids can be obtained by calibration and the critical flow pore size can be determined (Zhou et al., 2011; Guo et al., 2018). However, based on the principle of NMR, bound water still exists in throats larger than the critical flow diameter; thus, the critical flow diameter obtained by this method is small.

Cui et al. (2013) proposed the concept of the oil content (chloroform content per unit of sandstone). It can be used to determine the pore size corresponding to the oil content demarcation point, that is, the critical flow pore size. Ideally, when the pore is filled with oil or highly saturated, the oil content is linearly and positively correlated with the pore volume. However, in fact, not all pores can be effectively filled with oil. Therefore, if oil is stored in a pore throat with a diameter greater than a specific value, the oil content positively correlates with the pore volume with a diameter greater than that specific value. Based on this hypothesis, the correlation coefficient is positively correlated with the minimum oil pore size. When the correlation coefficient reaches the maximum value, the corresponding minimum oil pore size is the critical flow pore size (Wang et al., 2015).

Based on the wetting behavior of the solid–liquid interface at the nanoscale, the numerical simulation method of nanopore templates can be used to simulate and visualize the migration and reservoir processes of fluids in the nanopore templates with controllable pore shape and pore size, to study the occurrence of fluids in pores, and to determine the critical flow pore size (Zou et al., 2015).

With the development of shale oil and tight sandstone oil research, field emission scanning electron microscopy (FESEM) has been used to observe rock samples after argon ion polishing. It has been widely used to study the characteristics of pore throat structures at the micron–nanometer scale (Loucks et al., 2009, 2012; Milliken et al., 2013; Pommer and Milliken, 2015; Yang et al., 2016). In addition, commonly used pore structure test methods for unconventional reservoirs include low-pressure gas (N_2 and CO_2), low-temperature adsorption (Wang et al., 2015), high-pressure mercury injection (Hu et al., 2017), focused ion beam scanning electron microscopy (FIB-SEM; Curtis et al., 2012; Tang et al., 2016), NMR (Webber et al., 2013; Zhang et al., 2018), small-angle neutron scattering (Clarkson et al., 2011; Gu et al., 2015; Yang et al., 2017; Sun et al., 2018), nano-CT (Bai et al., 2013; Wu et al., 2015; Wang et al., 2016), nano-transmission X-ray photoelectron microscopy (Bernard et al., 2012), atomic force microscopy (Javadpour et al., 2012), and other methods. The rapid development of technology for tests in unconventional reservoirs provides powerful means for the study of mudstone caprock; new technology has been used for the evaluation of mudstone caprock sealing (Dewhurst et al., 2019).

In this paper, the shale caprock of the N gas reservoir of the

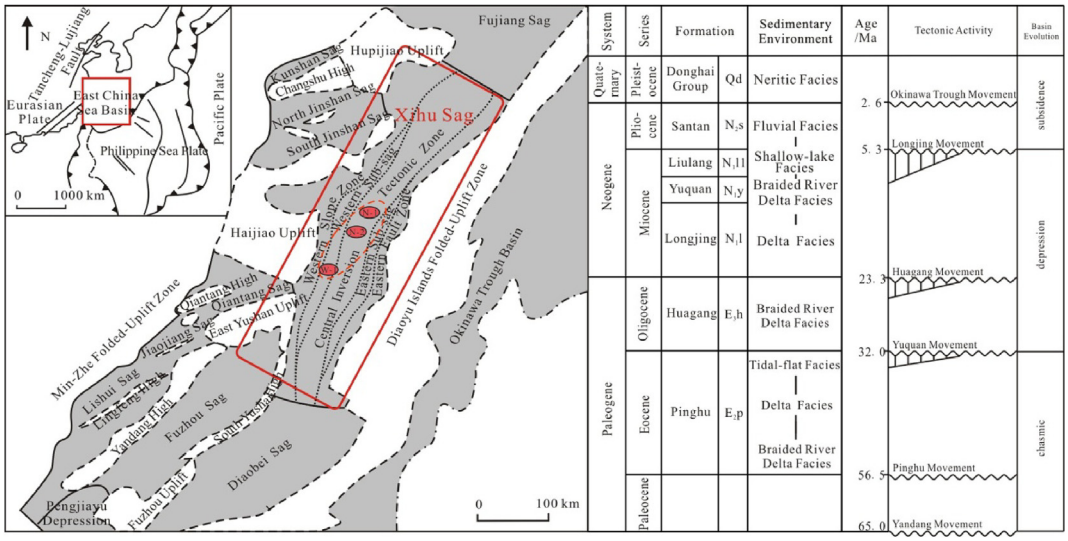

Fig. 1. Geological survey of the study area.

Huagang Formation in the Xihu sag, East China Sea Basin was studied by using new techniques for unconventional reservoir rock and mineral tests such as SEM, nano-CT, digital core reconstruction, low-temperature gas adsorption, high-pressure mercury intrusion, and NMR. The critical flow pore diameter of shale caprock was obtained by determining the boundary between the caprock and reservoir.

2. Geological setting

The East China Sea Basin is between the Min-Zhe and Diaoyu Islands folded uplift belts. It is the largest offshore petroleum basin in China. The Xihu sag is in the northeastern part of the basin. It has experienced a synrift period (from Cretaceous to Eocene), depression period (from Oligocene to Miocene), and regional subsidence period (from Pliocene to Quaternary). It can be divided into the western slope zone, western subsag, central inversion tectonic zone, eastern subsag, and eastern fault zone (Zhang and Zhang, 2015; Fig. 1). The strata consist of Palaeocene (E1); Eocene Pinghu (E2p) Formation; Oligocene Huagang (E3h) Formation, Miocene Longjing (N1l), Yuquan (N1y), and Liulang (N1ll) formations; Pliocene Santan (N2s) Formation; and Quaternary Donghai (Qd) group (Fig. 1). The N gas reservoir in the central inversion tectonic zone has a gentle structure and undeveloped faults. The trap type belongs to a large-scale broad–gentle anticline with high closure height and high gas filling degree. The buried depth of the gas reservoir is between 3000 and 4000 m. The upper part is a normal pressure system, while the lower part exhibits abnormal overpressure. The geothermal gradient is high, that is, ~3 °C/100 m–4°C/100 m. The primary source rocks are mainly the E2p Formation, which are buried between 3000 and 5000 m. They consist of dark mudstones and coal seams with thicknesses of > 200 and 20 m, respectively (Tao and Zou, 2005). The reservoirs are mainly developed in the E3h and E2p formations in the braided river delta, delta, and tidal flat facies. In this study, we focused on the upper E3h Formation in the western subsag and central inversion tectonic zone (Fig. 1). The primary regional caprocks are at the top of the E3h Formation. The caprock is a braided river delta floodplain deposit with strong heterogeneity. It is characterized by thin interbedded sand–mudstone, a large cumulative thickness, and an impure internal lithology including mudstone, silty mudstone, argillaceous siltstone, and siltstone, among which the silty mudstone and argillaceous siltstone dominate.

3. Material and method

3.1. Sample selection

The 360 m of shale caprock cores in the study area were finely described at the cm level and the sedimentary microenvironment of the shale caprock development was determined. In total, 118 samples were selected. The samples included at least one sample from each shale lithology. All samples were used for microscopic identification, particle size analysis, permeability and breakthrough pressure tests, ESEM, nano-CT tests, gas adsorption, high-pressure mercury injection, and NMR.

3.2. Lithology determination

The particle sizes of silt or sand in each shale sample were obtained by using the optical microscope and laser particle size analyzer. The shale lithology was determined based on the particle size (Milliken et al., 2012). The grain size range of clastic particles of the caprock is large, varying from clay to giant sand (< 0.0039–2 mm). However, the main proportion consists of fine to coarse silt (0.0039–0.0625 mm) according to the classification standard for the particle size of clastic particles (Table 1).

3.3. Permeability and breakthrough pressure test

For each shale sample without fractures, a standard plunger with a diameter of 2.5 cm and height of 5 cm was drilled perpendicular to the bedding direction. The permeability of each shale sample was obtained

Table 1
Classification standard for particle size of clastic particles.

size fraction	very coarse sand	coarse sand	medium sand	fine sand	very fine sand	Coarse silt	Medium silt	Fine silt	very fine silt	clay
particle diameter/mm	2–1	1–0.5	0.5–0.25	0.25–0.125	0.125–0.0625	0.0625–0.0312	0.0312–0.0156	0.0156–0.0078	0.0078–0.0039	< 0.0039

by the steady-state method. Based on the permeability test, the breakthrough pressure of each shale sample was determined under saturated kerosene conditions, room temperature, and at a confining pressure of 25 MPa using a breakthrough pressure test device.

3.4. Environmental scanning electron microscopy

For each shale lithology, a sample with a size of 2 cm × 2 cm × 0.5 cm was cut perpendicular to the bedding direction. The samples were manually polished using 600, 800, 1000, 1500 and 2000 mesh sandpaper. Subsequently, the argon ion profiler was used to polish the section. The prepared samples were subjected to secondary electron, backscattering, and energy spectrum analyses using ESEM to study the mineral composition and micropore structure of the shale lithology.

3.5. Nanometer-CT test and digital core reconstruction

To select specific shale samples, Oxford Lasers, a micromachining system were used to cut samples with diameters of up to 65 μm perpendicular to the bedding direction. Subsequently, Zeiss Xradia UltraXRM-L200 nano-CT equipment was used to scan every layer and 721 photos were obtained. Finally, Avizo software was utilized for digital core modeling to obtain a three-dimensional (3D) model of the pore structure of the shale caprock pores. The flow chart of the 3D modeling of the digital core is as follows.

(1) Data Import

The 721 images obtained by nano-scanning were imported into the Avizo digital core modeling software. The software automatically registered the images and slice arrangement, shear correction, and black spot correction were carried out. The real appearance of the core can be restored using a 3D view.

(2) Extraction of Volume Elements

Because of computer graphics card and processor limitations, it is necessary to extract a volume element. When choosing the volume element, not only the computer graphics card and processor were considered, but also the basic characteristics of shale caprock can be represented by the volume elements. The volume elements of 256 voxel × 256 voxel × 256 voxel were selected for the modeling.

(3) Noise Reduction Filtering

Because of the system noise or artifacts during nano-CT scanning, it is necessary to use an image filter to remove noise and enhance the image display. Commonly used filtering methods are median, bilateral, Sobel, and non-local median filtering. The non-local mean filter was used in this study, which preserves the image edges and effectively removes white noise.

(4) Threshold Segmentation

In nano-CT scanning, the gray levels of the final image differ because of the different conductivity of the components compared with the electrons. Based on the analysis of the histogram of the gray distribution in the image, the gray value of 8330 was selected as the threshold value and the image was divided into two parts. A gray value below 8330 represents the pores and other values represent the mineral skeleton.

(5) Interface Rendering

By rendering the interface of the segmented model, a smooth surface polygon is generated on the surface and the static 3D model of the shale pores can be obtained.

3.6. Gas adsorption and high-pressure mercury injection

Low-temperature gas adsorption and high-pressure mercury injection are important methods to quantitatively obtain the pore composition of shales. Low-temperature carbon dioxide adsorption, low-temperature nitrogen adsorption, and high-pressure mercury injection can be used to determine the micropore, mesopore, and macropore contents, respectively (Tian et al., 2012). In this study, the samples were divided into three equal parts according to the shale lithology. Using the automatic specific surface area and pore diameter distribution and mercury intrusion analyzers, low-temperature carbon dioxide and nitrogen adsorption and high-pressure mercury intrusion tests were carried out successively. The micropore, mesopore, and macropore contents of the samples were obtained. The full pore diameter distributions of each lithology of the shale caprock were finally obtained by superimposing the above-mentioned three contents.

3.7. Nuclear magnetic resonance test

The NMR was used to obtain the contents of movable and bound fluids in the core and to characterize the pore composition based on the T2 spectrum (Ge et al., 2014, 2015). By using the NMR core analyzer independently developed by the Shanghai Newmark Electronics Technology Company, the T2 spectrum of the sample saturated with distilled water was measured. Subsequently, the sample was centrifuged to remove the movable water and the T2 spectrum of the sample was measured again. The pore composition of the samples, including the movable and immovable water porosities, was obtained by comparing the two methods. The experimental conditions were as follows: the sample was saturated with distilled water and the experiment temperature was 25 °C. The acquisition parameters were the wait time of 6 s, the echo time of 0.3 ms, the repeated measurement times of 128, and the number of echoes of 4096.

4. Results and discussion

4.1. Breakthrough pressure limit

Breakthrough pressure is widely used in caprock sealing evaluation (Downey, 1984; He et al., 2017; Zhou et al., 2019). With respect to the determination of the critical flow pore size of mudstone caprock, the boundary between the reservoir and caprock is the primary issue, which is defined as the breakthrough pressure limit. The difference between the two lithologies is the pore structure, which results in different breakthrough pressures. Therefore, the breakthrough pressure is an effective index for the discrimination of the reservoir and caprock. The breakthrough pressure distribution in the reservoir and caprock and hydrocarbon-bearing conditions of the reservoirs can be used to determine the lower breakthrough pressure limit.

The test data for the N gas reservoir shows that the breakthrough pressure in > 97.7% of the sandstone reservoir is < 2 MPa. However, that of argillaceous caprock is generally > 2 MPa. The intersection point of the two trendlines is at ~2 Ma (Fig. 2). Therefore, the breakthrough pressure limit between the sandstone reservoir and mudstone caprock is 2 MPa.

The role of the caprock is to prevent hydrocarbon migration, leading to hydrocarbon accumulation in the reservoir. For a set of sandstone and shale, the reservoir can effectively capture oil and gas if the sealing ability of the overlying argillaceous caprock is higher than that of the underlying sandstone. In addition, more oil and gas can be captured when the sealing ability is higher; thus, the petroliferous properties are better. In contrast, the caprock has no sealing ability and oil and gas cannot be captured if the sealing ability of the overlying argillaceous

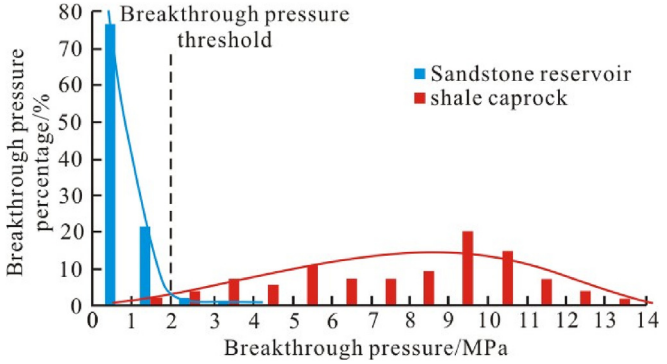

Fig. 2. The breakthrough pressure distribution of shale caprock and sandstone reservoir.

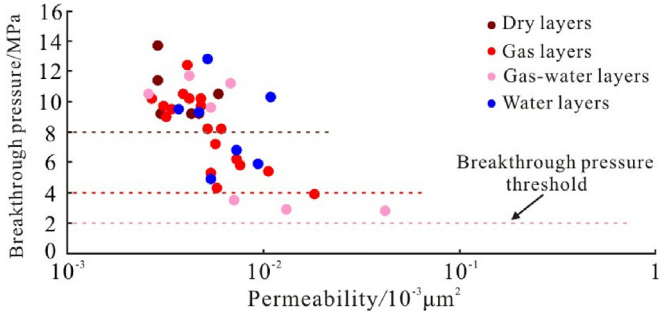

Fig. 3. The breakthrough pressure of direct shale caprock of different gas-bearing reservoir.

caprocks is close to or lower than that of the underlying sandstone. Therefore, the oil-bearing properties of a reservoir reflect the sealing ability of caprocks to a certain extent. Oil–water or gas–water layers play important roles in determining the breakthrough pressure limit of the reservoir and caprock. As the breakthrough pressure and sealing ability of the caprock decrease, the oil and gas dissipate and the hydrocarbon saturation gradually decreases. When the breakthrough pressure decreases to the extent that the caprock cannot seal oil and gas, the oil–water or gas–water layers will become water layers. Therefore, the lower breakthrough pressure limit of the caprocks of the oil–water or gas–water layers can be used as the breakthrough pressure limit of the reservoir and caprock. The N gas reservoir contains gas, gas–water, dry, and water layers. The lower breakthrough pressure limit of the caprocks of the gas, gas–water, and water layers is > 4 MPa, ~2 MPa, and < 2 MPa, respectively (Fig. 3). Therefore, it is reliable to consider the breakthrough pressure limit to be 2 MPa.

4.2. Critical lithology (particle size)

Because the capillary sealing ability of the caprock is mainly controlled by the pore structure, which mainly depends on the lithology, a good correlation exists between the breakthrough pressure and lithology based on the analysis of the breakthrough pressures of different lithologies in the study area. With the increase in the particle size, the sizes of the pores and throats increase and the pore structure improves. As a result, the breakthrough pressure and capillary sealing ability decrease (Fig. 4). Specifically, the granularity of the debris particles in silty mudstone and shaly fine–ultrafine siltstone is < 0.0156 mm, the breakthrough pressure is greater than 8 MPa, and the sealing ability is good. The clastic grain size of the argillaceous medium ranges from 0.0156 to 0.0312 mm, the minimum breakthrough pressure is 4 MPa, and the sealing ability is intermediate. The clastic grain size of argillaceous coarse siltstone ranges from 0.0312 to 0.0625 mm, the lower pressure limit of 2 MPa is exceeded, and the physical sealing ability is

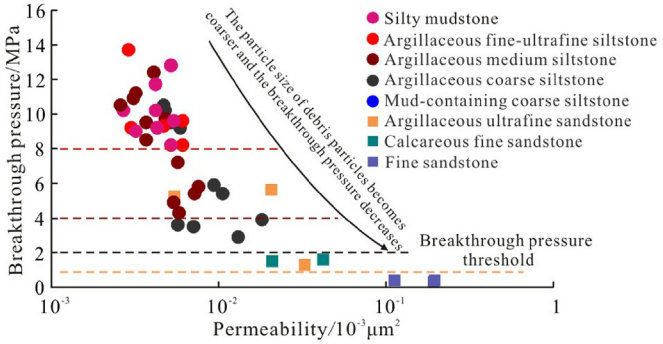

Fig. 4. The breakthrough pressure distribution of different lithologies.

poor. The grain size of the clastic grains of the extremely fine argillaceous sandstone ranges from 0.0625 to 0.125 mm, the breakthrough pressure ranges from 1 to 2 MPa, and the sealing ability is very poor. The clastic particle size of fine sandstone ranges from 0.125 to 0.25 mm, the breakthrough pressure is < 1 MPa. Fine sandstone has no sealing ability. However, the breakthrough pressure increases to ~1.5 MPa when the fine sandstone contains a small amount of calcareous cement (Fig. 4). The correlation between the breakthrough pressure and lithology shows that the lower breakthrough pressure limit of argillaceous coarse siltstone is ~2 MPa, which is consistent with the breakthrough pressure limit of the reservoir and caprocks. Therefore, argillaceous coarse siltstone can be used as critical lithology for the discrimination of the reservoir and caprocks. The minimum, average, and maximum breakthrough pressures of rocks with particle sizes smaller than that of argillaceous coarse siltstone, such as silty mudstone, shaly fine–ultrafine siltstone, and argillaceous medium siltstone, are greater than 2 MPa and the caprocks have a stronger capillary sealing ability. However, the minimum breakthrough pressures of rocks with particle sizes larger than that of argillaceous coarse siltstone, such as argillaceous very fine sandstone, calcareous sand stone, and fine sandstone, are < 2 MPa and the caprocks have a very poor or no capillary sealing ability (Fig. 5).

4.3. Critical flow pore diameter

The throat diameter is a critical parameter describing the pore structure and is closely related to the breakthrough pressure. After the rock samples were polished using argon ions, their mineral grain frameworks and planar characteristics of the pore structure can be clearly determined using FESEM. By using digital core technology-based nano-CT scans, the 3D mineral and pore structure can be reconstructed. Based on a combination of these two techniques, the microstructure of the rock can be accurately characterized. The two techniques have a

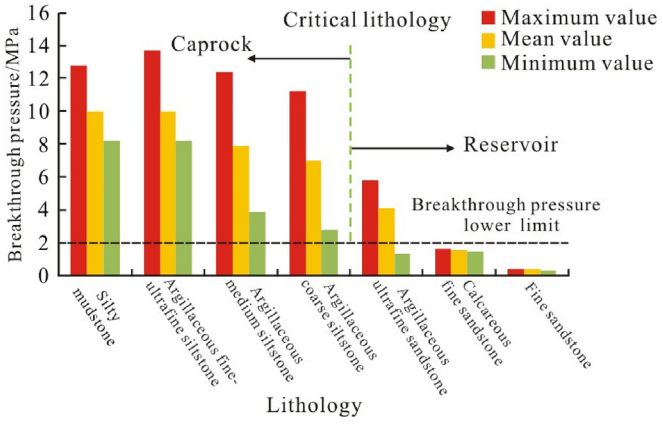

Fig. 5. The statistical results of breakthrough pressure of different lithologies.

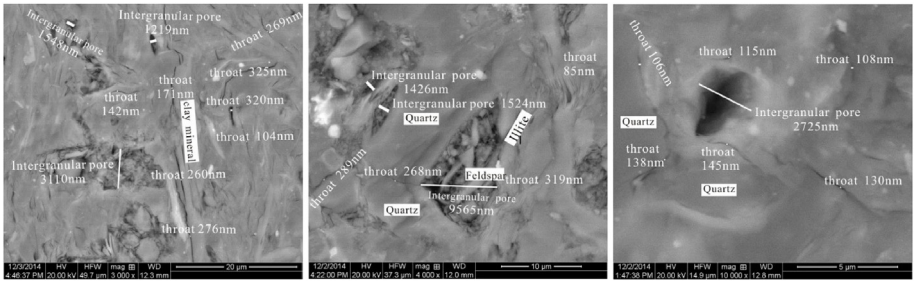

Fig. 6. The pore throat type and pore throat diameter of argillaceous coarse siltstone observed by SEM.

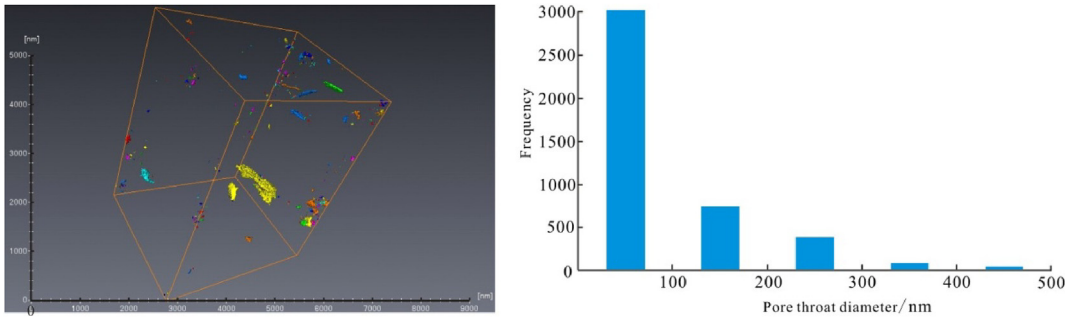

Fig. 7. The 3D digital model and statistical diameter of pore-throat of argillaceous coarse siltstone based on nano-CT scan.

nanometer-scale precision. Therefore, these techniques have been widely applied in studies of the pore structure of argillaceous rock (Teige et al., 2011; Zhang et al., 2016). Samples collected from the critical lithology (argillaceous coarse siltstone) have been observed using FESEM and 3D numerical rock construction has been carried out using nano-CT. The SEM observations show that the samples contain a small number of intergranular pores with large and micrometer-scale diameters. However, there are many throats connecting pores with diameters ranging from 85 to 325 nm, with an average of 198 nm (Fig. 6). The 3D digital model and statistics of the pore throat diameters indicate that the diameter of most of the nanoscale pore throats is less than 300 nm. The number of pore throats decreases with increasing pore throat diameter. This change is notable for diameters ranging from 100 to 300 nm (Fig. 7). Therefore, based on the SEM observations and the statistics of the 3D digital model, throats with diameters between 100 and 300 nm, with an average of 200 nm, have a significant effect on the pore structure of argillaceous coarse siltstone.

High-pressure mercury injection is a powerful tool to determine the critical pore flow diameter (Gong et al., 2015; Zhang et al., 2015). Mercury injection is a process during which liquid mercury breaks the pore throats in rock. Therefore, the mercury injection capillary pressure and corresponding amount of mercury injection reflect the pore structure of the rock and the breakthrough pore throat diameter. Based on the mercury intrusion curves and the corresponding breakthrough pore throat diameter of argillaceous coarse siltstone (Fig. 8), the process of mercury injection can be divided into three stages: macropore network breaking, pressure building, and mesopore network breaking. In the stage of macropore network breaking, the amount of injected mercury linearly correlates with the mercury injection capillary pressure, which shows that liquid mercury gradually breaks the connected pore throats under the mercury injection capillary pressure until breaking pore throats with diameters of 155 nm. Subsequently, the amount of injected mercury does not increase, although the mercury injection capillary pressure continues to increase. This indicates that the critical lithology lacks a pore throat network with diameters in the range of 12–155 nm or that this network is not connected to the macropore network. Therefore, the liquid mercury is in a pressure-building state. When the mercury injection capillary pressure continues to increase, the amount of mercury injection increases again, which shows that the liquid

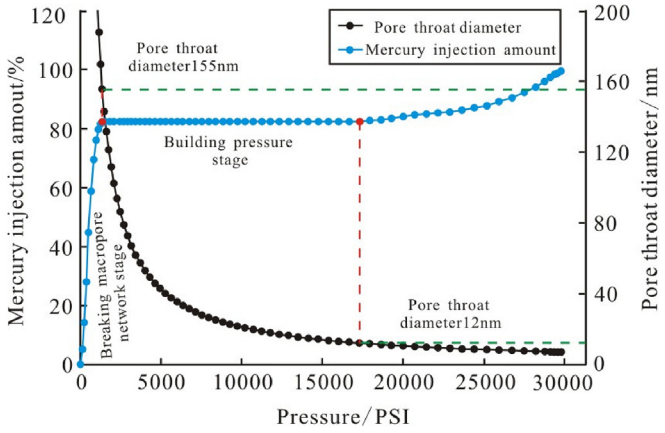

Fig. 8. The curves of mercury intrusion and breakthrough pore throat diameter of argillaceous coarse siltstone.

mercury begins to break the mesopore network with diameters below 12 nm. Therefore, the pore throats connecting the macropore and mesopore networks have diameters of 155 or 12 nm, respectively. However, when the liquid mercury breaks pore throats with diameters of 155 nm, the amount of mercury injection reaches 82.27%, which notably exceeds the amount criteria of mercury injection defining the breakthrough pressure. Therefore, the maximum connected pore throat diameter of argillaceous coarse siltstone is considered to be ≥ 155 nm. The critical throat diameter is ~200 nm based on the analysis of the breakthrough pressure limit (Figs. 9 and 10), calibrated throat diameter of argillaceous coarse siltstone, and statistical results for the average throat diameters of different lithologies. Rocks with particle sizes smaller than that of argillaceous coarse siltstone, such as silty mudstone and argillaceous medium siltstone, have a greater breakthrough pressure and smaller throat diameter. However, rocks with particle sizes larger than that of argillaceous coarse siltstone, such as argillaceous very fine sandstone, fine sandstone, and medium sandstone, have a breakthrough pressure smaller than 2 MPa and a throat diameter larger than 200 nm.

To further determine the critical throat diameter of caprock, the

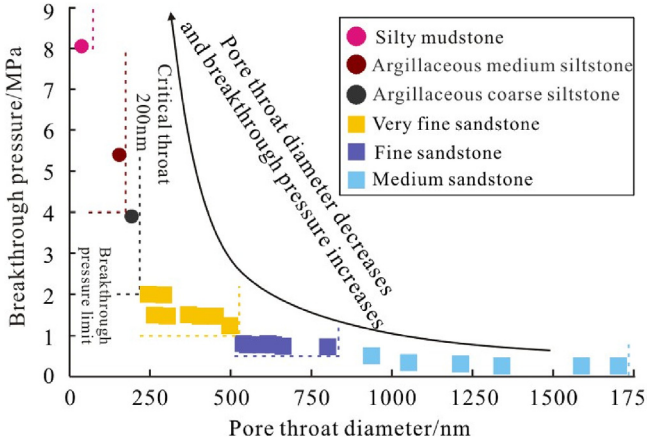

Fig. 9. The relationship plate of lithology-breakthrough pressure-pore throat diameter.

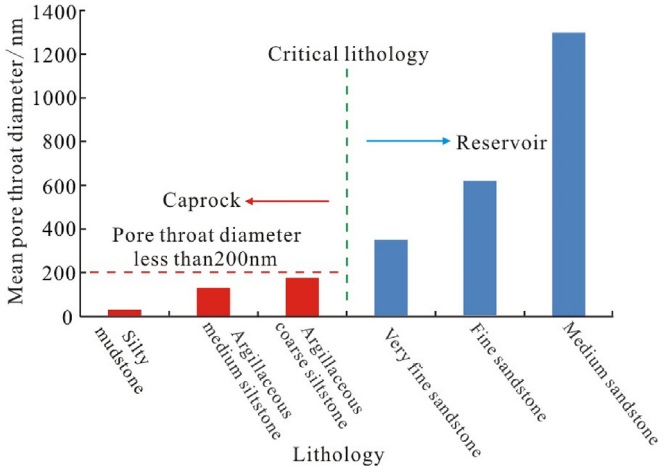

Fig. 10. The statistical result of average pore throat diameter of different lithologies.

distribution characteristics of three pore types (macropores, mesopores, and micropores) can be obtained by combining the high-pressure mercury injection with nitrogen and carbon dioxide adsorption experiments (Tian et al., 2012). The relaxation time (T2) NMR spectrum can be used to obtain the contents of movable and immovable fluids and indirectly reflects the pore structure. The joint mercury injection–gas adsorption experiment and NMR tests reflect the pore structure; therefore, the two test results are similar and comparable (Zhou et al., 2013; Li et al., 2015). The T2 NMR spectrum was calibrated using the pore structure obtained by the joint mercury injection–gas adsorption experiment. The pore size ranges of movable and immovable fluids can be quickly determined. The ratio of the pore sizes of these two fluids represents the pore size boundary of the movable fluid flowing in the fluid displacement experiment. When the pore size is lower than the ratio, the fluid is immovable. Even when the pressure increases, immovable fluid cannot flow. This shows that the rock has a capillary sealing ability from the sealing point. Therefore, the ratio of the pore sizes of the movable and immovable fluids can be used as critical throat diameter of the caprock capillary sealing. The average pore size should be less than this ratio for rocks with a physical sealing capacity. The critical lithology, that is, argillaceous coarse sandstone, was selected to carry out the above-mentioned tests. Fig. 11a shows the pore size distribution curve obtained from the joint mercury injection–gas adsorption experiment, displaying micropore sizes ranging from 0.3 to 1.5 nm; mesopore sizes ranging from 3.0 to 13 nm; and macropore sizes ranging from 50 to 84 nm, 148–339 nm, and

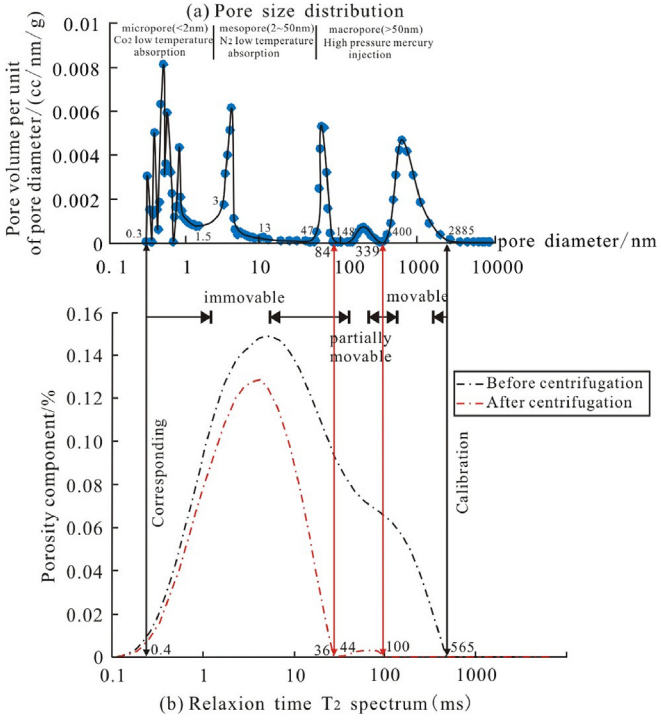

Fig. 11. The correlation analysis between pore size and relaxation time T2 spectrum of argillaceous coarse siltstone.

400–2885 nm. Fig. 11b shows the relaxation time T2 NMR spectrum; the black solid line represents the spectrum before centrifuging the samples, with T2 in the range of 0.1–565 ms, and the red dotted line represents the spectrum after centrifuging the samples, with T2 ranging from 0.1 to 36 ms and 44–100 ms. The comparison of the pore size distribution curve with the T2 spectrum of the same sample shows that they are in good agreement. The spectrum before centrifuging the samples is due to fluid from all micropores, mesopores, and macropores. However, the spectrum after centrifuging the samples is due to fluid from all micropores, mesopores, and macropores in the range of 47–84 nm and some macropores in the range of 148–339 nm. The corresponding relations indicate that all the fluids in the macropores with sizes of 400–2885 nm were separated and became movable after centrifuging the samples. Some fluids in the macropores with sizes of 148–339 nm were separated and became movable. However, fluids in pore throats with sizes below 84 nm could not be separated and are immovable. This is consistent with the thick (86 nm) immovable water film between the particles that was calculated using a theoretical model (Xiang et al., 1999; Yang et al., 2013). Based on the pore size distribution and comparison of the T2 spectra before and after centrifuging the samples, the critical throat diameter is larger than 84 nm, ranging from 148 to 339 nm.

4.4. Significance of the critical flow pore diameter in unconventional reservoirs

The critical flow pore diameter has important practical implications for the evaluation of the fluid mobility of shale oil and gas (Sun et al., 2016). The shale reservoir matrix has a nm–μm-scale pore structure, resulting in bad physical properties. Therefore, artificial fracturing is needed to achieve commercial production. Nevertheless, the shale oil and gas production of single wells rapidly decreases and the stable production time is very short. Therefore, the intrinsic permeability of the shale matrix is the key factor determining the continuous supply of oil and gas molecules to fractures to achieve long-term stable production. However, the permeability of the shale matrix is ultimately

controlled by the pore diameter. The critical flow pore diameter is usually used to evaluate whether shale oil and gas can flow in pores. When the pore diameter is larger than the critical flow pore diameter, oil and gas can flow freely and continuously; otherwise, it cannot flow. However, because the pore diameters of micropores are mainly at the nm–μm scale, it is difficult to directly test the fluid mobility using experimental methods (Tian et al., 2012; Zhang et al., 2019). Based on the multi-scale seepage characteristics of shale (Javadpour et al., 2007), without considering diffusion and slippage, the mobility of free oil and gas in the pore structure based on continuous flow can be divided into two types: flow in single pores and flow in the multi-scale pore structure of the rock. The lower pore diameter limit of oil and gas flowing in a single pore is very low, that is, at the nanometer scale (Wang et al., 2016). Therefore, oil and gas can flow in a single nanoscale pore, but flow may not occur in the actual pore structure or the rock has been fractured. The flow of oil and gas in the multi-scale pore structure under the driving forces of fluid overpressure and capillary force is a process of continuously breaking through smaller pore diameters, similar to the test processes of the displacement pressure in the reservoir and breakthrough pressure in the caprock. Because the core plug is at the cm scale and contains the complete pore structure of the shale lithology, it should be the basic unit of shale studies. Therefore, the critical flow pore diameter obtained from the core plug based on the shale lithology is very important for oil and gas to break through the whole multi-scale pore network, which is more realistic.

In addition to the evaluation of the shale caprock sealing and fluid mobility, the critical flow pore diameter can also be used for the prediction of the fluid overpressures of different shale lithologies. The pore diameter is the key to the formation of capillary pressure, while the nanopores in shale have a large adsorption resistance. Both cause fluid overpressure. The calculation equations are as follows (Lv et al., 2000):

$$P_s = 2P_o + P_c, \tag{1}$$

$$P_c = \frac{2\sigma\cos\theta}{r}, \tag{2}$$

where P_s is the maximum sealing capacity of shale with a certain lithology, Pa; P_o is the maximum fluid overpressure developing in shale with a certain lithology, Pa; P_c is the displacement pressure of shale with a certain lithology, that is, the capillary pressure corresponding to the critical flow pore diameter of the shale, Pa; σ is the interfacial tension of the fluid, N/m; θ is the wetting angle, °; and r is the maximum radius of the connected pore and throat, m.

In addition, the maximum sealing capacity of shale with a certain lithology can be obtained from the fracture pressure based on the true triaxial mechanical test of the rock or the leak-off test of formation:

$$P_s = P_f, \tag{3}$$

where P_f is the fracture pressure of shale with a certain lithology, Pa.

The maximum fluid overpressure developing in shale with a certain lithology can be obtained by combining Eqs (1)–(3):

$$P_o = \frac{1}{2}(P_f - P)_c = \frac{1}{2}\left(P_f - \frac{2\sigma\cos\theta}{r}\right) \tag{4}$$

For the shale with a certain lithology, the fracture pressure of the shale is obtained from the true triaxial mechanical test, the displacement pressure of the shale is obtained from the critical flow pore diameter, and the maximum fluid overpressure developing in the shale is calculated using Eq. (4). This provides a method for predicting the fluid overpressure in different shale lithologies, which is helpful to guide the drilling and production in shale reservoirs. Taking the critical lithology of argillaceous coarse siltstone in the study area as an example, the calculation of the maximum fluid pressure that may develop is introduced in detail.

The critical flow pore diameter of argillaceous coarse siltstone is 200 nm, the interfacial tension between formation water and gas is 72 × 10-3 N/m, and the wetting angle is 135°. Then displacement pressure of 1 MPa is obtained by using capillary pressure of Eq. (2).

$$P_c = \frac{2\sigma\cos\theta}{r} = \frac{2 \times 72 \times 10^{-3} N/\ \mathrm{m} \times \cos 135°}{100 \times 10^{-9}\mathrm{m}} \approx 1\mathrm{MPa} \tag{5}$$

The fracture pressure of argillaceous coarse siltstone obtained by the true triaxial mechanical test under the formation conditions is 67 Mpa, that is, the maximum sealing capacity of argillaceous coarse siltstone.

$$P_f = P_s = 67\mathrm{MPa} \tag{6}$$

The maximum fluid pressure of 33 MPa that may develop in the argillaceous coarse siltstone is obtained by substituting Eqs (5) and (6) into Eq. (4).

$$P_o = \frac{1}{2}\left(P_f - P_c\right) = \frac{1}{2}\left(67\mathrm{MP\ a} - 1\mathrm{MPa}\right) = 33\mathrm{MPa} \tag{7}$$

5. Conclusions

Based on the calibration of the breakthrough pressure distribution of the reservoir and the lower breakthrough pressure limit of the gas–water layer, the breakthrough pressure limit between the shale caprock and sandstone reservoir in the Huagang Formation in the Xihu Depression is 2 MPa. Based on the correlation between the breakthrough pressure and lithology, the lower breakthrough pressure limit of argillaceous coarse siltstone is 2 MPa. Therefore, argillaceous coarse siltstone can be used as the critical lithology to distinguish the shale caprock and sandstone reservoir of the Huagang Formation in the Xihu Depression. Based on the breakthrough pressure limit and calibration using the critical lithology, the critical throat diameter of the caprocks of the N gas reservoir was determined to be 200 nm for using a variety of methods including SEM, nano-CT, high-pressure Hg injection, gas adsorption experiments, and NMR. Lithologies with throat diameters smaller than 200 nm generally have a capillary sealing ability and belong to the caprock.

Acknowledgements

This work was supported by the Natural Science Foundation of China (Grant No. 41802172; 41830431), National Science Technology Major Project of China (Grant No. 2017ZX05009-001), Natural Science Foundation of Shandong Province of China (Grant No. ZR2018BD014) and Fundamental Research Funds for the Central Universities of China (Grant No. 18CX02178A).

References

Alyafei, N., Blunt, M.J., 2018. Estimation of relative permeability and capillary pressure from mass imbibition experiments[J]. Adv. Water Resour. 115, 88–94.
Bai, B., Zhu, R., Wu, S., Cui, J., Su, L., Li, T., 2014. New micro-throat structural characterization techniques for unconventional tight hydrocarbon reservoir[J]. China Pet. Explor. 19 (3), 78–86.
Bai, B., Zhu, R., Wu, S., Yang, W., Gelb, J., Gu, A., Zhang, X., Su, L., 2013. Multi-scale method of Nano (Micro)-CT study on microscopic pore structure of tight sandstone of Yanchang Formation, Ordos Basin[J]. Pet. Explor. Dev. 40 (3), 354–358.
Bernard, S., Horsfield, B., Schulz, H.M., Wirth, R., Schreiber, A., Sherwood, N., 2012. Geochemical evolution of organic-rich shales with increasing maturity: a STXM and TEM study of the Posidonia Shale (Lower Toarcian, northern Germany)[J]. Mar. Pet. Geol. 31 (1), 70–89.
Cao, Q., Zhao, J., Liu, X., Hu, A., Fan, L., Wang, H., 2013. Determination of physical property limits for the gas accumulation in tight sandstone reservoirs in the eastern Ordos Basin[J]. Acta Pet. Sin. 34 (6), 1040–1048.
Clarkson, C.R., Freeman, M., He, L., Agamalian, M., Melnichenko, Y.B., Mastalerz, M., Bustin, R.M., Radliński, A.P., Blach, T.P., 2011. Characterization of tight gas reservoir pore structure using USANS/SANS and gas adsorption analysis[J]. Fuel 95, 371–385.
Cui, J., Zhu, R., Wu, S., Wang, T., 2013. Heterogeneity and lower oily limits for tight sandstones: a case study on Chang-7 oil layers of the Yanchang Formation, Ordos Basin[J]. Acta Pet. Sin. 34 (5), 877–882.
Curtis, M.E., Sondergeld, C.H., Ambrose, R.J., Rai, C.S., 2012. Microstructural investigation of gas shales in two and three dimensions using nanometer-scale resolution imaging microstructure of Gas Shales. AAPG (Am. Assoc. Pet. Geol.) Bull. 96 (4), 665–677.

Deng, Y., Ren, Z., Ma, W., Chen, X., Yang, G., Nanka, E., 2018. Reservoir properties and hydrocarbon charging threshold of Chang 8 tight sandstones in Fuxian area, Ordos Basin[J]. Pet. Geol. Exp. 40 (2), 288–294.
Dewhurst, D.N., Delle Piane, C., Esteban, L., Sarout, J., Josh, M., Pervukhina, M., Clennell, M.B., 2019. Microstructural, geomechanical, and petrophysical characterization of shale caprocks. Geol. Carbon Storage 1–30.
Downey, M.W., 1984. Evaluating seals for hydrocarbon accumulation. AAPG (Am. Assoc. Pet. Geol.) Bull. 68 (11), 1752–1763.
Gao, Y., Jiang, Y., Yang, C., Cheng, F., 2011. Minimum flow pore throat radius for determination of the lower limits of parameters in low permeability reservoir[J]. Sci. Technol. Rev. 29 (4), 34–38.
Ge, X., Fan, Y., Li, J., Zahid, M.A., 2015. Pore structure characterization and classification using multifractal theory—an application in Santanghu basin of western China. J. Pet. Sci. Eng. 127, 297–304.
Ge, X., Fan, Y., Zhu, X., Chen, Y., Li, R., 2014. Determination of nuclear magnetic resonance T2 cutoff value based on multifractal theory—an application in sandstone with complex pore structure[J]. Geophysics 80 (1), D11–D21.
Gee, M.L., McGuiggan, P.M., Israelachvili, J.N., Homola, A.M., 1990. Liquid to solid like transitions of molecularly thin films under shear[J]. J. Chem. Phys. 93 (3), 1895–1906.
Gong, Y., Liu, S., Zhu, R., Liu, K., Tang, Z., Jiang, L., 2015. Lower limit of tight oil flowing porosity: application of high-pressure mercury intrusion in the fourth Member of Cretaceous Quantou Formation in southern Songliao Basin, NE China. Pet. Explor. Dev. 42 (5), 745–752.
Gu, X., Cole, D.R., Rother, G., Mildner, D.F., Brantley, S.L., 2015. Pores in Marcellus shale: a neutron scattering and FIB-SEM study[J]. Energy Fuels 29 (3), 1295–1308.
Guo, R., Chen, X., Ma, X., Ma, J., Wang, Q., Chen, L., 2018. Analysis of the characteristics and its influencing factors of horizontal movable fluid in the Chang 7 tight reservoir in Longdong area,Ordos Basin. Nat. Gas Geosci. 29 (5), 665–674.
He, C., Hua, M., 1998. The thickness of water-film in oil and gas reservoirs[J]. Pet. Explor. Dev. 25 (2), 75–77.
He, Z.L., Li, S.J., Wo, Y.J., Zhang, D.W., Gu, Y., Zhou, Y., 2017. Major factors controlling hydrocarbon preservation condition in the marine basins of China and its evaluation ideas. Acta Petrol. Sin. 33 (4), 1221–1232.
Hu, Q.H., Liu, H., Yang, R., Zhang, Y.X., Kibria, G., Sahi, S., Alatrash, N., Macdonnell, M.M., Chen, W., 2017. Applying molecular and nanoparticle tracers to study wettability and connectivity of Longmaxi Formation in southern China[J]. J. Nanosci. Nanotechnol. 17 (9), 6284–6295.
Hu, Y., Yu, X., Chen, G., Li, S., 2012. Classification of the average capillary pressure function and its application in calculating fluid saturation[J]. Pet. Explor. Dev. 39 (6), 778–784.
Javadpour, F., Fisher, D., Unsworth, M., 2007. Nanoscale gas flow in shale gas sediments. J. Can. Pet. Technol. 46 (10), 55–61.
Javadpour, F., Farshi, M.M., Amrein, M., 2012. Atomic-force microscopy: a new tool for gas-ghale characterization. J. Can. Pet. Technol. 51 (4), 236–243.
Jiao, C., Xia, D., Wang, J., Liu, L., Sheng, W., Cheng, P., 2009. Methods for determining the petrophysical property cutoffs of extra-low porosity and permeability sandstone reservoirs-an example from the Xishanyao Formation reservoirs in Yongjin oilfield. Oil Gas Geol. 30 (3), 379–383.
Leverett, M.C., 1941. Capillary behavior in porous solids. Trans. AIME 142, 151–169.
Li, A., Ren, X., Wang, G., Wang, Y., Jiang, K., 2015. Characterization of pore structure of low permeability reservoirs using a nuclear magnetic resonance method. J. China Univ. Pet. (Ed. Nat. Sci.) 39 (6), 92–98.
Li, Y., Sima, L., Yan, J., Yang, L., 2014. Determination of petrophysical property cutoffs of tight sandstone gas reservoirs: a case study of T3x2 gas reservoirs in P area of central Sichuan Basin. Nat. Gas. Ind. 34 (4), 52–56.
Liu, X., Liu, X., Zhao, H., Wang, H., Zhang, H., 2016. A new method to calculate the lower limit of effective pore throat threshold of tight sandstone reservoirs: a case study of he-8 gas reservoir in sulige gas field. Xinjing Pet. Geol. 37 (3), 360–364.
Loucks, R.G., Reed, R.M., Ruppel, S.C., Hammes, U., 2012. Spectrum of pore types and networks in mudrocks and a descriptive classification for matrix-related mudrock pores. AAPG Bull. 96 (6), 1071–1098.
Loucks, R.G., Reed, R.M., Ruppel, S.C., Jarvie, D.M., 2009. Morphology, genesis, and distribution of nanometer-scale pores in siliceous mudstones of the Mississippian Barnett Shale. J. Sediment. Res. 79 (12), 848–861.
Lu, X., Liu, K., Zhuo, Q., Zhao, M., Liu, S., Fang, S., 2012. Palaeo-fluid evidence of the multi-stage hydrocarbon charges in Kela-2 gas field, Kuqa foreland basin, Tarim Basin [J]. Pet. Explor. Dev. 39 (5), 574–582.
Lv, Y., Fu, G., Zhang, F., Fu, X., Wang, X., 2000. Quantitative study on sealing ability of ultra-pressure caprock. Acta Sedimentol. Sin. 18 (3), 465–468.
Milliken, K.L., Esch, W.L., Reed, R.M., Zhang, T., 2012. Grain assemblages and strong diagenetic overprinting in siliceous mudrocks, Barnett shale (mississippian), Fort Worth basin, Texas. AAPG (Am. Assoc. Pet. Geol.) Bull. 96 (8), 1553–1578.
Milliken, K.L., Rudnicki, M., Awwiller, D.N., Zhang, T., 2013. Organic matter-hosted pore system, Marcellus formation (Devonian), Pennsylvania. AAPG (Am. Assoc. Pet. Geol.) Bull. 97 (2), 177–200.
Pommer, M., Milliken, K., 2015. Pore types and pore-size distributions across thermal maturity, Eagle Ford Formation, southern Texas. AAPG (Am. Assoc. Pet. Geol.) Bull. 99 (9), 1713–1744.
Purcell, W.R., 1949. Capillary pressures-their measurement using mercury and the calculation of permeability therefrom[J]. Trans. AIME 186, 39–48.
Ren, Y., Wu, K., He, K., Wu, G., Zhu, Y., Wu, H., Yang, Y., 2017. Application of NMR technique to movable fluid of ultra-low permeability and tight reservoir : a case study on the yanchang formation in longdong area, ordos basin[J]. J. Mineral. Petrol. 37 (1), 103–110.
Stout, J.L., 1964. Pore geometry as related to carbonate stratigraphic traps[J]. AAPG (Am. Assoc. Pet. Geol.) Bull. 48 (3), 329–337.
Sun, C., Yao, S., Li, J., Liu, B., 2016. The characterization of shale oil reservoir in Dongying Sag[J]. Geol. Rev. 62 (6), 1497–1510.
Sun, M., Yu, B., Hu, Q., Yang, R., Zhang, Y., Li, B., Melnichenko, Y.B., Cheng, G., 2018. Pore structure characterization of organic-rich Niutitang shale from China: small angle neutron scattering (SANS) study[J]. Int. J. Coal Geol. 186, 115–125.
Tang, X., Jiang, Z., Jiang, S., Li, Z., 2016. Heterogeneous nanoporosity of the Silurian Longmaxi Formation shale gas reservoir in the Sichuan Basin using the QEMSCAN, FIB-SEM, and nano-CT methods[J]. Mar. Pet. Geol. 78, 99–109.
Tao, S.Z., Zou, C.N., 2005. Accumulation and distribution of natural gases in Xihu sag, East China Sea Basin. Pet. Explor. Dev. 32, 103–110.
Teige, G.M.G., Hermanrud, C., Rueslatten, H.G., 2011. Membrane seal leakage in non-fractured caprocks by the formation of oil-wet flow paths[J]. J. Pet. Geol. 34, 45–52.
Tian, H., Zhang, S., Liu, S., Zhang, H., 2012. Determination of organic-rich shale pore features by mercury injection and gas adsorption methods[J]. Acta Pet. Sin. 33 (3), 419–427.
Wang, G., Ju, Y., Yan, Z., Li, Q., 2015. Pore structure characteristics of coal-bearing shale using fluid invasion methods: a case study in the Huainan–Huaibei Coalfield in China [J]. Mar. Pet. Geol. 62, 1–13.
Wang, M., Yang, J., Wang, Z., Lu, S., 2015. Nanometer-scale pore characteristics of lacustrine shale, Songliao Basin, NE China. PLoS One 10 (8), e0135252.
Wang, P., Jiang, Z., Chen, L., Yin, L., Li, Z., Zhang, C., Tang, X., Wang, G., 2016. Pore structure characterization for the Longmaxi and Niutitang shales in the Upper Yangtze Platform, South China: evidence from focused ion beam–He ion microscopy, nano-computerized tomography and gas adsorption analysis[J]. Mar. Pet. Geol. 77, 1323–1337.
Wang, S., 2009. Analysis of rock pore structural characteristic by nuclear magnetic resonance[J]. Xinjing Pet. Geol. 30 (6), 768–770.
Wang, S., Javadpour, F., Feng, Q., 2016. Molecular dynamics simulations of oil transport through inorganic nanopores in shale[J]. Fuel 171, 74–86.
Webber, J.B.W., Corbett, P., Semple, K.T., Ogbonnaya, U., Teel, W.S., Masiello, C.A., Fisher, Q.J., Valenza II, J.J., Song, Y., Hu, Q., 2013. An NMR study of porous rock and biochar containing organic material[J]. Microporous Mesoporous Mater. 178, 94–98.
Wu, S., Zhu, R., Cui, J., Cui, J., Bai, B., Zhang, X., Jin, X., Zhu, D., You, J., Li, X., 2015. Characteristics of lacustrine shale porosity evolution, Triassic Chang 7 member, Ordos Basin, NW China[J]. Pet. Explor. Dev. 42 (2), 185–195.
Xiang, Y., Xiang, D., Yang, Y., Zhang, C., Liu, C., 1999. Study of gas recovery and water film thickness in water drive for tight sandstone gas reservoir[J]. J. Chengdu Univ. Technol. (Sci. Technol. Ed.) 26 (4), 389–391.
Yan, J., Zhang, F., Hu, Q., Wang, J., Geng, B., Tang, H., Dong, Z., 2018. Pore structure and effectiveness of low-permeability reservoirs on the south slope of Dongying depression. J. China Univ. Min. Technol. 47 (2), 345–356.
Yang, H., Li, S., Liu, X., 2013. Characteristics and resource prospects of tight oil and shale oil in Ordos Basin[J]. Acta Pet. Sin. 34 (1), 1–14.
Yang, R., He, S., Hu, Q., Sun, M., Hu, D., Yi, J., 2017. Applying SANS technique to characterize nano-scale pore structure of Longmaxi shale, Sichuan Basin (China)[J]. Fuel 197, 91–99.
Yang, R., He, S., Yi, J., Hu, Q., 2016. Nano-scale pore structure and fractal dimension of organic-rich Wufeng-Longmaxi shale from Jiaoshiba area, Sichuan Basin: investigations using FE-SEM, gas adsorption and helium pycnometry[J]. Mar. Pet. Geol. 70, 27–45.
Zhou, Y., Wei, G., Guo, H., 2011. Impact factors analysis and decision tree correction of NMR porosity measurements[J]. Well Logging Technol. 35 (3), 210–214.
Zou, C., Jin, X., Zhu, R., Gong, G., Sun, L., Dai, J., Meng, D., Wang, X., Li, J., Wu, S., Liu, X., Wu, J., Jiang, L., 2015. Do shale pore throats have a threshold diameter for oil storage? Sci. Rep. 5, 13619.
Zou, C., Yang, Z., Cui, J., Zhu, R., Hou, L., Tao, S., Yuan, X., Wu, S., Lin, S., Wang, L., Bai, B., Yao, J., 2013. Formation mechanism, geological characteristics and development strategy of nonmarine shale oil in China. Pet. Explor. Dev. 40 (1), 15–27.
Zou, C., Zhu, R., Bai, B., Yang, Z., Wu, S., Su, L., Dong, D., Li, X., 2011. First discovery of nano-pore throat in oil and gas reservoir in China and its scientific value[J]. Acta Petrol. Sin. 27 (6), 1857–1864.
Zhang, G.H., Zhang, J.P., 2015. A discussion on the tectonic inversion and its genetic mechanism in the East China Sea Shelf Basin. Earth Sci. Front. 22, 260–270.
Zhang, H., Zhang, S., Liu, S., Hao, J., Zhao, M., Tian, H., Jiang, L., 2014a. A theoretical discussion and case study on the oil-charging throat threshold for tight reservoirs[J]. Pet. Explor. Dev. 41 (3), 408–416.
Zhang, H., Liu, S., Zhang, S., Gong, Y., Hao, J., Tian, H., 2014b. Discussion on oil-charging threshold of throat in tight sandstone in gongshanmiao oilfield, sichuan and its application[J]. Nat. Gas Geosci. 25 (5), 693–700.
Zhang, L., Guo, J., Tang, H., Liu, J., Li, Q., He, J., 2015. Pore structure characteristics of Longmaxi shale in the southern Sichuan Basin[J]. Nat. Gas. Ind. 35, 22–29.
Zhang, P., Lu, S., Li, J., 2019. Characterization of pore size distributions of shale oil reservoirs: a case study from Dongying sag, Bohai Bay basin, China[J]. Mar. Pet. Geol. 100, 297–308.
Zhang, P., Lu, S., Li, J., Chen, C., Xue, H., Zhang, J., 2018. Petrophysical characterization of oil-bearing shales by low-field nuclear magnetic resonance (NMR)[J]. Mar. Pet. Geol. 89, 775–785.
Zhang, Q., Liang, F., Pang, Z., Jiang, S., Zhou, S., Zhang, J., 2019. Lower threshold of pore-throat diameter for the shale gas reservoir: experimental and molecular simulation study[J]. J. Pet. Sci. Eng. 173, 1037–1046.
Zhang, Q., Liu, R., Pang, Z., Lin, W., Bai, W.H., Wang, H.Y., 2016. Characterization of microscopic pore structures in Lower Silurian black shale (S1l), southeastern Chongqing, China[J]. Mar. Pet. Geol. 71, 250–259.
Zhou, H., Gao, F., Zhou, X., Liu, H., Guo, B., Wang, C., 2013. The translation research of different types sandstone of Yungang Grottoes in NMR T2-mercury capillary pressure [J]. Prog. Geophys. 28 (5), 2759–2766.
Zhou, X., Lv, X., Quan, H., Qian, W., Mu, X., Chen, K., Wang, Z., Bai, Z., 2019. Influence factors and an evaluation method about breakthrough pressure of carbonate rocks: an experimental study on the Ordovician of carbonate rock from the Kalpin area, Tarim Basin, China. Mar. Pet. Geol. 104, 313–330.